Self-consistent relativistic band structure of the $CH_3NH_3PbI_3$ perovskite

E. Menéndez-Proupin,[1,2] P. Palacios,[3] P. Wahnón,[1] and J. C. Conesa[4]
[1]*Instituto de Energía Solar and Dept. TEAT, E.T.S.I. Telecomunicación, Universidad Politécnica de Madrid, Spain*
[2]*Departamento de Física, Facultad de Ciencias, Universidad de Chile, Casilla 653, Santiago, Chile*
[3]*Instituto de Energía Solar and FyQATA, E.I. Aeronáutica y del Espacio, Universidad Politécnica de Madrid*
[4]*Instituto de Catálisis y Petroleoquímica, CSIC, Marie Curie 2, 28049 Madrid, Spain*
(Received 27 February 2014; revised manuscript received 9 July 2014; published 24 July 2014)

The electronic structure and properties of the orthorhombic phase of the $CH_3NH_3PbI_3$ perovskite are computed with density functional theory. The structure, optimized using a van der Waals functional, reproduces closely the unit cell volume. The experimental band gap is reproduced accurately by combining spin-orbit effects and a hybrid functional in which the fraction of exact exchange is tuned self-consistently to the optical dielectric constant. Including spin-orbit coupling strongly reduces the anisotropy of the effective mass tensor, predicting a low electron effective mass in all crystal directions. The computed binding energy of the unrelaxed exciton agrees with experimental data, and the values found imply a fast exciton dissociation at ambient temperature. Also polaron masses for the separated carriers are estimated. The values of all these parameters agree with recent indications that fast dynamics and large carrier diffusion lengths are key in the high photovoltaic efficiencies shown by these materials.

DOI: 10.1103/PhysRevB.90.045207 PACS number(s): 88.40.J−, 71.20.−b, 88.40.H−

I. INTRODUCTION

Organic and inorganic perovskites have gained strong interest as photon absorbers in thin-film solar cells. With the first prototypes demonstrated five years ago [1], current cell efficiencies have surpassed the 15% barrier [2–5].

Methyl ammonium lead iodide ($CH_3NH_3PbI_3$) is one of the most attractive integrants of this family. $CH_3NH_3PbI_3$ presents a characteristic perovskite structure consisting of a network of PbI_6^- octahedra, with Pb^{2+} cations at the center and I^- anions at the corners. The octahedra are connected through the corners (see Fig. 1), and the cavities in between are occupied by monovalent cations, $CH_3NH_3^+$. The large size and aspherical shape of $CH_3NH_3^+$ cause distortions in the network and drive several phase transitions related to the orientation of the $CH_3NH_3^+$ ion. For temperatures below 160 K, the structure presents an orthorhombic crystal symmetry (group nr. 62, *Pnma*), and the $CH_3NH_3^+$ cations have a definite orientation [6], as shown in Fig. 1. Between 162.2 and 327.4 K the framework symmetry is tetragonal and the $CH_3NH_3^+$ cations keep rotating and jumping between several equivalent orientations consistent with the crystal symmetry [6–9]. For $T > 327.4$ K, the disorder of the $CH_3NH_3^+$ cations increases, and the framework of PbI_6^- octahedra adopts an average cubic symmetry [6–8].

The understanding and improvement of this family of solar absorbers needs a collaboration of experiments and simulations. Considering the complex phase diagram and the interplay between the structural distortions and optoelectronic properties, it is desirable to achieve high accuracy in the simulations. Early calculations in the framework of density functional theory (DFT) showed a good agreement of theoretical band gap with the experimental determinations (see [6] and references therein). However, this agreement results from the cancellation between the well-known gap underestimation error in the standard DFT generalized gradient approximation (GGA) and the neglect of the spin-orbit (SO) interaction, which when included reduces the gap in these systems by 1 eV [12]. Agreement with experiment has been recently demonstrated using many-body GW calculations, including relativistic effects, on top of DFT [13,14]. Hybrid functionals that include a fraction of exact exchange, such as PBE0 [15,16] and HSE [17,18] generally increase the band gap, counteracting the mentioned underestimation error, and improve the agreement of the predictions with the experimental band gap of semiconductors [19]. Hybrid functionals share formal and practical similarities with the GW Coulomb-hole and screened-exchange (COHSEX) approximation [20,21], and their use is currently easier and more extended than that of GW.

Here, the band structure of the $CH_3NH_3PbI_3$ orthorhombic phase has been computed using hybrid functionals and including the SO interaction. The functionals HSE and PBE0 have been used in the calculations, as well as PBE0 with an optimized value of the fraction of exact exchange. Section II describes the computational framework used. Section III presents the structural properties and band structure. Section IV discusses the experimental data and presents estimations of effective masses including polaron effects. Section V is devoted to our concluding remarks.

II. METHODS

The calculations have been performed using the Vienna *ab initio* simulation package (VASP) [22]. Ion-electron interaction and scalar relativistic effects are included in the projector augmented waves approximation (PAW) [23,24]. The standard PAW potentials have been used for H, I, and Pb elements, and soft potentials for C and N. For variable cell relaxations, a plane-wave cutoff of 364 eV has been used, which is 30% higher than the maximum cutoff for nitrogen. For band calculations, the maximum default cutoff (280 eV) was used. Test calculations were performed with hard PAW potentials for carbon and nitrogen, which have a maximum cutoff of 400 eV. With these hard PAW potentials, variable cell relaxation gave a cell volume only 2% larger than with soft

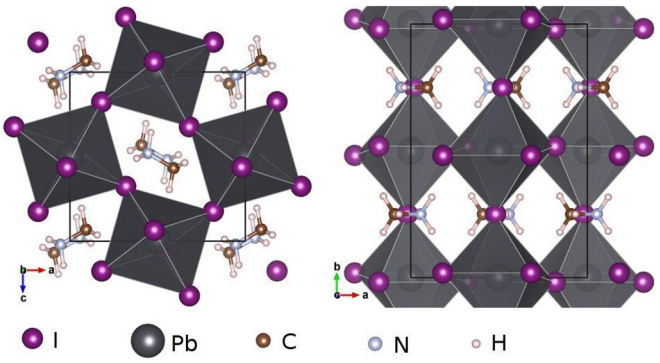

FIG. 1. (Color online) Optimized structure of $CH_3NH_3PbI_3$.

potentials, and the C-N bond distance variation is smaller than 0.01 Å. The Brillouin zone has been sampled using $3 \times 2 \times 3$ Γ-centered grids for calculations with GGA functionals, and $2 \times 2 \times 2$ for hybrid functionals. Tests were made for k-point grids up to $7 \times 5 \times 8$, showing that the $2 \times 2 \times 2$ grid allows the total energy converged within 0.01 eV/atom, and the pressures are converged within 1 kbar. For the $3 \times 2 \times 3$ grid the total energy is converged within 1 meV/atom. The band gap at the Γ point is converged within 0.02 eV for the $2 \times 2 \times 2$ grid.

It has been proposed on the basis of GW-type theory and checked for several semiconductors [21,25–29] that for the PBE0 functional, the optimal fraction of exact exchange to reproduce band gaps can be determined as $\alpha = 1/\epsilon_\infty$, where ϵ_∞ is the electronic (high-frequency) dielectric constant, which should be computed in self-consistency with α [27]. In the present work, the dielectric constant has been obtained computing the electric polarization under an external electric field, by means of the Berry phase theory [30–32]. We call this method PBE0α+SO. We have obtained self-consistently the values $\alpha = 0.188$ and $\epsilon_\infty = 5.32$. Our ϵ_∞ is somewhat smaller than previous DFT results in the range 5.69–6.29 [14,33], and larger than the GW result [14] $\epsilon_\infty^{\mathrm{GW}} = 4.5$. The difference between DFT values can be attributed to differences in the band gaps obtained with different functionals and the treatment of the SO coupling. The GW value $\epsilon_\infty^{\mathrm{GW}} = 4.5$ was obtained with SO coupling and using the random-phase approximation, where local field effects are usually neglected. As can be seen in Sec. II.3 of Ref. [30], the same approximation with the standard PBE0 functional gives $\epsilon_\infty = 4.6$. Hence, our larger value 5.32 is likely due to the inclusion of local field effects in the Berry-phase calculation. An experimental value $\epsilon_\infty^{\mathrm{expt}} = 6.5$ has been estimated from diffuse reflection measurements [34,35].

III. RESULTS

A. Structural properties

The hydrogen positions are not resolved by x-ray-based crystallographic experimental techniques [6,8] and must be obtained by simulations. For the tetragonal and cubic phases, the disorder in the orientation of the C-N bond raises the difficulty level for theoretical techniques. A simplified technique, applied in several studies, has the $CH_3NH_3^+$ cation substituted by more symmetrical cations, such as Cs^+ or NH_4^+, or even eliminated from the calculations [6,33]. This method is certainly useful and has allowed researchers to prove that the states associated with the cation have little effect on the band structure around the gap [6]. However, the nature of the cation modifies the structure of the different phases and influences strongly the transition temperatures. Therefore, $CH_3NH_3^+$ should not be substituted by other cations when the structure is optimized by simulation. In this work, we aim at an accurate description of the geometrical and electronic structure of the ordered low-temperature orthorhombic phase.

As said above, the experimental determinations of the crystallographic structure [6] do not resolve the hydrogen positions. Hence, the hydrogen coordinates have been placed in appropriate starting positions compatible with the space group of the low-temperature phase and the structure has been fully relaxed. As the ions in this structure can undergo van der Waals interaction, three density functionals including dispersion interactions [10,11] have been used for the structural relaxation, as well as the PBE functional [36]. The lattice parameters optimized with different functionals are compared in Table I. The optB88-vdW and optB68b-vdW functionals are seen to provide the best agreement with the crystallographic parameters, confirming their capability for solid-state applications [11]. Interatomic distances show the same trend as lattice parameters, with the exception of the C-N bond distance. The experimental C-N bond length, 1.57 Å, is anomalously (0.05–0.09 Å) larger than our simulation optimized lengths. This may be due to the fact that the x-ray diffraction technique assigns the atom positions to the centers of gravity near the maxima of the electronic density distribution, which for CH_3 and NH_3 groups may deviate from the exact positions of the C and N atoms. Auxiliary calculations for the isolated cation $CH_3NH_3^+$ show that the optimized C-N bond length is close to the values of Table I, either with GGA or with hybrid functionals. Hence, no effect from the inorganic framework is evident from simulations. Let us note

TABLE I. Lattice parameters, bond distances, and cell volumes obtained from variable cell relaxation starting from the experimental structure. Units are Å and Å^3.

	PBE	vdW-DF2[a]	optB88-vdW[a]	optB86b-vdW[a]	Expt[b]
Volume	1008.8	1046.6	952.46	945.28	951.01
a	9.177	9.132	8.827	8.806	8.836
b	12.816	13.137	12.679	12.633	12.580
c	8.577	8.724	8.510	8.498	8.555
b/a	1.397	1.439	1.436	1.435	1.424
c/a	0.935	0.955	0.964	0.965	0.968
d(C-N)	1.49	1.52	1.50	1.50	1.571
d(I-Pb)	3.23	3.29	3.19	3.19	3.174
	3.24	3.30	3.20	3.19	3.175
	3.26	3.31	3.22	3.21	3.180
d(H-I)	2.58	2.66	2.56	2.56	
	2.60	2.66	2.58	2.58	

[a]Van der Waals functionals: vdW-DF2 (Ref. [10]), optB88-vdW, and optB86b-vdW (Ref. [11]).
[b]Reference [6].

TABLE II. Structure of $CH_3NH_3PbI_3$ optimized with the van der Waals density functional optB88-vdW.

Space group 62 (*Pnma*)			
Lattice vectors: $a = 8.8273$ Å, $b = 12.6793$ Å, $c = 8.5099$ Å			
Fractional coordinates:			
Pb	0.00000	0.00000	0.50000
I	0.98041	0.25000	0.56319
I	0.18148	0.01821	0.17644
C	0.40839	0.25000	0.43168
N	0.55516	0.25000	0.51975
H	0.11881	0.31686	0.01029
H	0.15523	0.82116	0.96378
H	0.03804	0.25000	0.85812
H	0.93323	0.25000	0.19489

that for $CH_3ND_3PbBr_3$, the C-N experimental bond distance, measured in this case with neutron diffraction, is reported as 1.48 Å [37]; and for $CH_3NH_3PbI_3$ at the room-temperature phase [8], determined with x-ray diffraction, the C-N distance is 1.39 Å.

For the following calculations of the electronic structure, the geometric configuration obtained with the functional optB88-vdW has been employed. The coordinates of nonequivalent atoms in the unit cell are given in Table II.

B. Electronic structure

Figure 2 shows the band structure and gaps obtained with several GGA and hybrid functionals without and with SO coupling. The band energies are given relative to the averaged electrostatic potential, which is a useful reference for interface and defect calculations [25,26,38] and is less sensitive than the band edges to the choice of exchange-correlation functional. More complete band diagrams are given in [30]. As illustrated for the PBE functional, the SO coupling modifies strongly the bottom of the conduction band (CB) and reduces the band gap by 0.9 eV, in agreement with Ref. [12]. The same reduction takes place with hybrid functionals (see a summary in Table III). Maybe more important than the precise gap values is the SO effect on the topology of the CB. The lowest CBs, which at the Γ point are grouped in a range of 1 eV in the calculation without SO, become more dispersive and are more separated at every k point when the SO is switched on. The SO coupling also causes some avoided crossings. On the other hand, including a fraction of Hartree-Fock exchange increases the band gap and also increases the dispersion of the valence bands, while the CB shape remains with little changes. Figure S5 in Ref. [30] shows the PBE + SO results after a scissors shift superimposed with the HSE + SO and PBE0α + SO bands. It can be appreciated that the scissors shift after the PBE + SO calculation provides a good approximation to the bands, although the valence band is 0.5–0.6 eV narrower than with hybrid functionals. The conduction band is also narrower in PBE + SO, although the effect is less significant than for the valence band. Figure S5 also shows that by transitive relation, HSE + SO and PBE0α + SO bands are also similar to each other, the more important difference being the band gap values, which change from 1.37 to 1.63 eV.

The standard procedure in VASP for band calculations with hybrid functionals failed for PBE0α+SO and PBE0 + SO. Instead, the band energies shown in Fig. 2 were taken from fully self-consistent calculations using regular Γ-centered grids with augmented density along the symmetry lines, i.e., $14 \times 2 \times 2$ and $2 \times 10 \times 2$ for the X-Γ and Γ-Y lines, respectively. The band energies actually computed with PBE0α+SO are shown by circles in Fig. 2 and are joined by spline lines, while for the other functionals, 40 k points were computed along every symmetry line.

It can be appreciated that going from PBE to the hybrid functionals, the downward offset of the valence band maximum (VBM) is much larger than the upward offset of the conduction band minimum (CBM), giving the larger contribution to the gap opening. The downward shift affects all the valence bands, which also get wider.

Figure 3 shows the total (DOS) and the projected density of states (PDOS). It can be seen that around the fundamental band gap, only iodine and lead orbitals contribute to the DOS. The bands from organic molecular levels are almost isolated

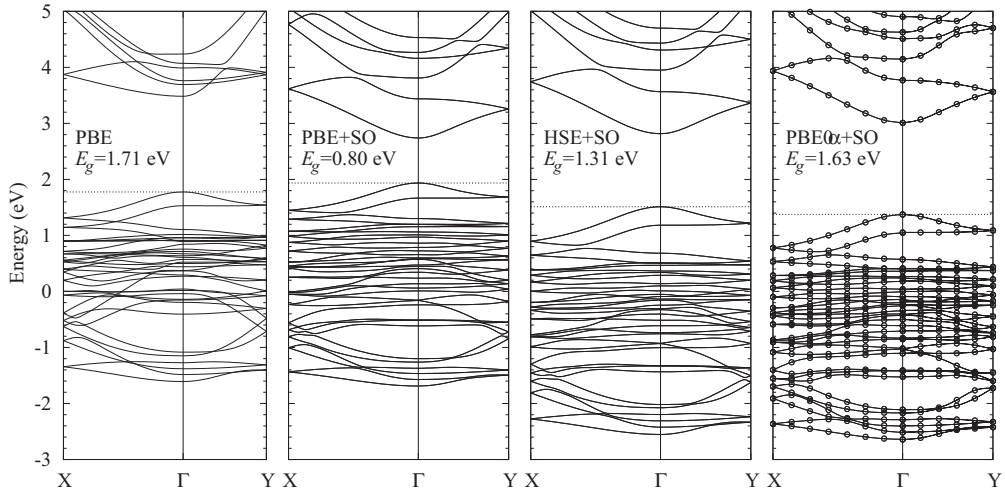

FIG. 2. Band diagram of $CH_3NH_3PbI_3$ computed with different functionals. The structure is optimized with functional optB88-vdW. The energy zero is the average electrostatic potential, and the valence band maximum is indicated with a dotted line.

TABLE III. Band parameters obtained from different exchange-correlation functionals: the band gap E_g, the energies of the conduction band minimum (E_{CBM}) and valence band maximum (E_{VBM}), and the valence band width (Δ_{VBW}). E_{CBM} and E_{VBM} are relative to the average electrostatic potential. Δ_{VBW} is measured between E_{VBM} and the minimum of the bands shown in Fig. 2. All values are in eV units.

	PBE	PBE+SO	HSE	HSE+SO	PBE0	PBE0+SO	PBE0α	PBE0α+SO
E_g	1.71	0.80	2.27	1.31	2.89	1.92	2.59	1.63
E_{VBM}	1.78	1.94	1.36	2.82	1.03	1.19	1.22	1.38
E_{CBM}	3.48	2.74	3.62	1.51	3.92	3.11	2.59	3.01
Δ_{VBW}	3.38	3.62	3.83	4.06	3.90	4.14	3.78	4.02

at −4.3, −6.3, −8.5, −12.6, and −19.9 eV. Some interaction with the levels of the inorganic framework is appreciated by very small contributions of Pb and I PDOS at the first three energies. The inorganic framework dominates the bands at −18.0, −15.4, −11.2, and −7.0 eV, the top valence band in the range from −2.6 to −1.4 eV, and the band from −7.5 to −6.5 eV. The latter mixes with the organic band at −6.3 eV.

It is useful to evaluate if the spin-orbit coupling can be calculated in perturbation theory instead of self-consistently, as there are codes that implement only the first option, while offering an efficient algorithm for hybrid functionals. It would be also relevant for comparing with one-shot (non-self-consistent) GW calculations [13], or with perturbative spin-orbit within self-consistent GW [14]. To obtain this approximation in VASP, the band diagram has been computed without the spin-orbit interaction, followed by a single iteration of the self-consistent cycle with the spin-orbit calculation.

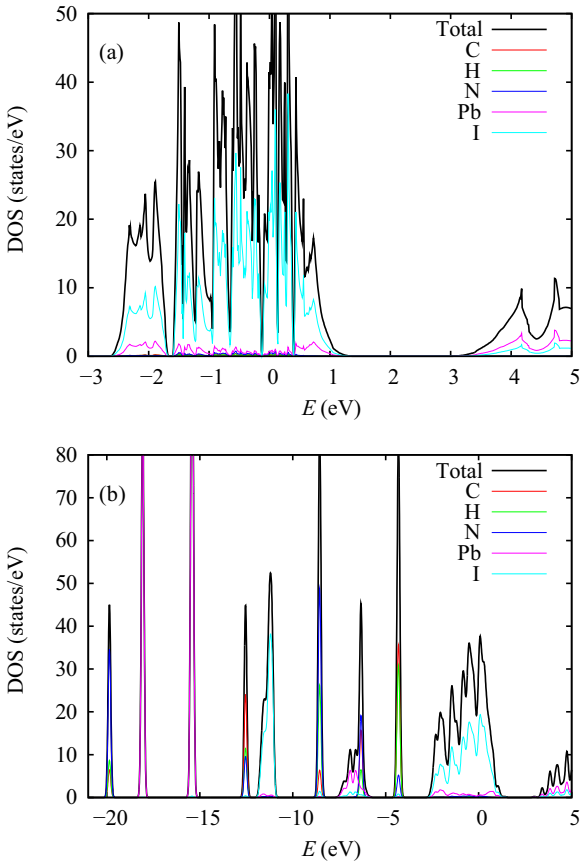

FIG. 3. (Color online) Density of states of $CH_3NH_3PbI_3$ computed with PBE0α+SO.

The resulting band diagram is almost equal to the fully self-consistent SO calculation. Figure 4 shows superimposed bands calculated perturbatively and self-consistently. The bands are quite similar in both schemes, being the larger difference in the higher valence band, causing a rise of the HSE gap from 1.31 to 1.37 eV. For energies higher than 2 eV or smaller than −2 eV, the differences are smaller.

IV. DISCUSSION

The band gap of $CH_3NH_3PbI_3$ at low temperature has been estimated as 1.68 eV [39]. Our results indicate that the best match is provided by the PBE0α + SO calculation, with the α value computed self-consistently as explained above.

Although the band gap values with PBE0α + SO and plain PBE (without SO) are similar, Fig. 2 and Table III show that the offsets of both VBM and CBM relative to the electrostatic potential which are given by PBE deviate significantly from those given by PBE0α + SO (which is presumably more accurate). Those PBE offsets are in the first case, respectively, ca. 0.40 and 0.47 eV larger than those found with the second functional. This should be taken into account when computing band alignments at interfaces, position of defect levels relative to the bands, or band offsets relative to the vacuum level.

Table IV presents the effective mass tensors of the highest valence and the lowest conduction band edges. m_{xx} and m_{yy} correspond to Γ-X and Γ-Y directions, respectively. It can be appreciated that missing the SO coupling the effective mass presents high anisotropy. The anisotropy is very reduced when

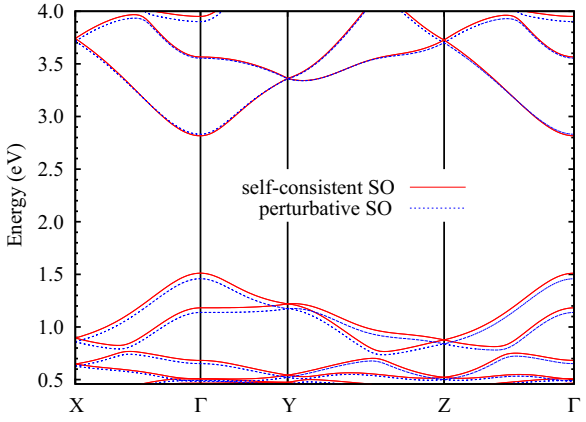

FIG. 4. (Color online) Band diagram of $CH_3NH_3PbI_3$ computed with HSE + SO, where the SO interaction is computed self-consistently and perturbatively. The energy zero is the average electrostatic potential.

TABLE IV. Effective masses (in units of the free electron mass) and ranges of the isolated conduction band and the top valence band. $\Delta_{c,v}$ are the ranges where the corresponding bands do not overlap with the next bands.

	PBE	PBE+SO	HSE+SO
		Conduction band	
m_{xx}	0.70	0.18	0.20
m_{yy}	0.088	0.13	0.15
m_{zz}	1.00	0.19	0.22
$\langle m_c \rangle$[a]	0.22	0.17	0.18
Δ_c(eV)	0.23	0.50	0.52
		Valence band	
$-m_{xx}$	0.29	0.22	0.23
$-m_{yy}$	0.23	0.18	0.21
$-m_{zz}$	0.28	0.22	0.23
$\langle m_h \rangle$[a]	0.26	0.21	0.22
Δ_v(eV)	0.23	0.25	0.29

[a] $\langle m_{c,h} \rangle = 3|\sum_i 1/m_{ii}|^{-1}$.

SO is included, and the masses are similar for all functionals. This agrees with the observation that the scissors shift after the PBE + SO calculation provides a good approximation to the band shapes near the gap. The parameters Δ in Table IV are the energy ranges that the lowest CB and the top VB span as isolated bands, which are important for the validity of the effective mass approximation [40]. The length of the Γ-Y path is 0.24 Å^{-1}; which is the largest extension in a reciprocal state that can have a nonperiodic electronic state [40] to be described within the one-band effective mass approximation. For the fitting of the effective masses, a range of 0.057 Å^{-1} around the Γ point has been used. Out of this range, roughly one quarter of the Γ-Y path, the band nonparabolicity increases the apparent effective masses. The averaged electron and hole masses are slightly smaller than those calculated in Ref. [41] using PBE and PBE + SO and a pseudocubic model of the room-temperature phase. The difference is consistent with the larger Pb-I distances and smaller mass density of their model, optimized without van der Waals attractions, an omission that partially compensates for the thermal expansion. The same argument applies for comparison with the effective masses reported in Ref. [13], which were calculated for a low symmetry of the tetragonal room-temperature phase. The decrease of anisotropy was also obtained in Ref. [13]. Note that these electron effective masses are not significantly higher than those measured for other typical semiconductors used in photovoltaic (PV) cells, while the hole masses are smaller than for the same semiconductors.

Taking the average masses of the HSE + SO approximation, a reduced exciton mass of $\mu = 0.099$ is obtained. Using the dielectric constant ϵ_∞, the exciton binding energy and Bohr radius (in the Wannier-Mott model [42]) are $\mu e^4/2\hbar^2\epsilon_\infty^2 =$ 48 meV and $\hbar^2\epsilon_\infty/\mu e^2 = 28$ Å. These values are appropriate for the exciton appearing immediately after photon absorption, i.e., when no atomic relaxation has occurred yet. This binding energy agrees with the experimental value of ca. 50 meV [43] obtained from optical absorption spectra. A similar value has been obtained recently [44] for the $CH_3NH_3PbI_{3-x}Cl_x$ mixed halide perovskite in the neighborhood of room temperature. Excitonic effects are therefore small enough that the optically determined band gap can be used for the comparison with the band structure calculation. On the other hand, for a sufficiently large exciton lifetime, i.e., longer than the characteristic time of atomic vibrations, one should consider the atomically relaxed exciton, which is likely the state from which either electron-hole dissociation or recombination can occur. For this situation the Wannier-Mott model should include the static dielectric constant (see Ref. [45] for additional arguments in favor of using it); with the average of values reported in Ref. [33], $\epsilon_0 = 25.7$, a radius of 137 Å and a binding energy of 2 meV are obtained. This latter value implies that the exciton will be dissociated for temperatures over 30 K.

For transport properties, relevant after exciton dissociation, polaron masses must be considered rather than the bare electronic masses computed with fixed ions. They can be estimated using the Fröhlich's continuum theory of the large polaron [46], which predicts a polaron to bare mass ratio $m_p/m = 1 + \alpha_p/6$. The coupling constant is $\alpha_p = \sqrt{me^4/2\hbar^2\epsilon_*^2 E_{\rm LO}}$, where $E_{\rm LO}$ is the energy of the longitudinal optical phonon, and $1/\epsilon_* = 1/\epsilon_\infty - 1/\epsilon_0$. Using the values $E_{\rm LO} = 38.4$ meV [47], $\epsilon_\infty/\epsilon_0 = 0.235$ [33], and the HSE + SO effective masses, we obtain 0.21 and 0.27 for the electron and hole polaron masses, respectively. The polaron energy shifts, $\Delta E_p = -\alpha_p E_{\rm LO}$, are -49 and -44 meV for the hole and the electron, respectively.

Our results differ somewhat from recent calculations for $CH_3NH_3PbI_3$ that include the SO interaction. Lang *et al.* [48] still underestimated the gap using HSE + SO. Brivio *et al.* [14] used a self-consistent GW approach and achieved a good agreement with the experimental gap. However, their band diagram shows anisotropy in valence and conduction band dispersion around the point R, which is folded into Γ for our supercell. Also, they obtained nonanalytic dispersions of the bands around R, and several extremal points. It is difficult to assess if this is a many-body effect or a result of an uncontrolled approximation of the spin-orbit coupling, e.g., the neglect of the spin off-diagonal terms. More probably, the differences with our results are due to different symmetries of the structural models, which in Refs. [14,48] are restricted to cubic lattices and smaller units cell; and, in addition, the dipoles of all $CH_3NH_3^+$ cations point in these models in the same direction, which may lead to fictitious internal electric fields affecting the electronic structure. Our large and variable supercell has more freedom to relax, and the tilting and rotation of the PbI_6 polyhedra is rather large, as is appreciated in Fig. 1. This argument seems to be confirmed by our agreement with GW result for the 48-atom supercell [13].

V. CONCLUSIONS

We have shown that DFT calculations with hybrid functionals (preferably PBE0α) and spin-orbit coupling are able to reproduce the experimental band gap of $CH_3NH_3PbI_3$, as well as other relevant parameters like the reduced mass and binding energy of the optically observed exciton. Hybrid functional DFT is less costly than GW and we have been able to study a relatively large supercell. This opens the way to computing the electronic structure of $CH_3NH_3PbI_3$ at room temperature using large supercells that can include

the dynamical and orientational disorder of the $CH_3NH_3^+$ cations. $CH_3NH_3PbI_3$ adds to the list of semiconductors where the PBE0α provides the best accuracy for computing the fundamental band gap [21,25–27,29], when the fraction α of the Hartree-Fock exchange is chosen as the inverse of the high-frequency dielectric constant computed self-consistently. We also show that the spin-orbit interaction modifies strongly the effective mass tensor of the conduction band, which is derived from the Pb 6*p* orbitals; if neglected, the conduction band presents very high effective mass in certain directions. With spin-orbit included, the conduction band becomes almost isotropic and the effective mass gets closer to the range typical of classical II–VI semiconductors. The low binding energy value obtained for the exciton predicts its easy dissociation, which differs from the behavior of organic PV absorbers.

ACKNOWLEDGMENTS

This work was supported by the European Project NANOCIS of the FP7-PEOPLE-2010-IRSES and DEF-HYDFT (SOPHIA project). The authors thankfully acknowledge the computer resources, technical expertise, and assistance provided by the Madrid Supercomputing and Visualization Center (CeSViMa) and the Jülich Supercomputing Centre (JSC).

[1] A. Kojima, K. Teshima, Y. Shirai, and T. Miyasaka, J. Am. Chem. Soc. **131**, 6050 (2009).
[2] G. Hodes, Science **342**, 317 (2013).
[3] M. Liu, M. B. Johnston, and H. J. Snaith, Nature **501**, 395 (2013).
[4] J. Burschka, N. Pellet, S.-J. Moon, R. Humphry-Baker, P. Gao, M. K. Nazeeruddin, and M. Grätzel, Nature **499**, 316 (2013).
[5] J. T.-W. Wang, J. M. Ball, E. M. Barea, A. Abate, J. A. Alexander-Webber, J. Huang, M. Saliba, I. Mora-Sero, J. Bisquert, H. J. Snaith *et al.*, Nano Lett. **14**, 724 (2014).
[6] T. Baikie, Y. Fang, J. M. Kadro, M. Schreyer, F. Wei, S. G. Mhaisalkar, M. Graetzel, and T. J. White, J. Mater. Chem. A **1**, 5628 (2013).
[7] O. Knop, R. E. Wasylishen, M. A. White, T. S. Cameron, and M. J. M. van Ooort, Can. J. Chem. **68**, 412 (1990).
[8] C. C. Stoumpos, C. D. Malliakas, and M. G. Kanatzidis, Inorg. Chem. **52**, 9019 (2013).
[9] Y. Kawamura, H. Mashiyama, and K. Hasebe, J. Phys. Soc. Jpn. **71**, 1694 (2002).
[10] K. Lee, E. D. Murray, L. Kong, B. I. Lundqvist, and D. C. Langreth, Phys. Rev. B **82**, 081101 (2010).
[11] J. Klimeš, D. R. Bowler, and A. Michaelides, Phys. Rev. B **83**, 195131 (2011).
[12] J. Even, L. Pedesseau, J.-M. Jancu, and C. Katan, J. Phys. Chem. Lett. **4**, 2999 (2013).
[13] P. Umari, E. Mosconi, and F. De Angelis, Sci. Rep. **4**, 4467 (2014).
[14] F. Brivio, K. T. Butler, A. Walsh, and M. van Schilfgaarde, Phys. Rev. B **89**, 155204 (2014).
[15] J. P. Perdew, M. Ernzerhof, and K. Burke, J. Chem. Phys. **105**, 9982 (1996).
[16] C. Adamo and V. Barone, J. Chem. Phys. **110**, 6158 (1999).
[17] J. Heyd, G. E. Scuseria, and M. Ernzerhof, J. Chem. Phys. **118**, 8207 (2003).
[18] J. Heyd, G. E. Scuseria, and M. Ernzerhof, J. Chem. Phys. **124**, 219906 (2006).
[19] M. Marsman, J. Paier, A. Stroppa, and G. Kresse, J. Phys.: Condens. Matter **20**, 064201 (2008).
[20] J. Paier, M. Marsman, K. Hummer, G. Kresse, I. C. Gerber, and J. G. Ángyán, J. Chem. Phys. **124**, 154709 (2006).
[21] M. A. L. Marques, J. Vidal, M. J. T. Oliveira, L. Reining, and S. Botti, Phys. Rev. B **83**, 035119 (2011).
[22] G. Kresse and J. Furthmüller, Phys. Rev. B **54**, 11169 (1996).
[23] P. E. Blöchl, Phys. Rev. B **50**, 17953 (1994).
[24] G. Kresse and D. Joubert, Phys. Rev. B **59**, 1758 (1999).
[25] A. Alkauskas, P. Broqvist, and A. Pasquarello, Phys. Status Solidi B **248**, 775 (2011).
[26] J. C. Conesa, J. Phys. Chem. C **116**, 18884 (2012).
[27] J. C. Conesa, Catal. Today **208**, 11 (2013).
[28] T. Le Bahers, M. Rérat, and P. Sautet, J. Phys. Chem. C **118**, 5997 (2014).
[29] J. H. Skone, M. Govoni, and G. Galli, Phys. Rev. B **89**, 195112 (2014).
[30] See Supplemental Material at http://link.aps.org/supplemental/10.1103/PhysRevB.90.045207 for details on the calculations and additional information on the electronic structure.
[31] R. W. Nunes and X. Gonze, Phys. Rev. B **63**, 155107 (2001).
[32] I. Souza, J. Íñiguez, and D. Vanderbilt, Phys. Rev. Lett. **89**, 117602 (2002).
[33] F. Brivio, A. B. Walker, and A. Walsh, APL Mater. **1**, 042111 (2013).
[34] M. Hirasawa, T. Ishihara, T. Goto, K. Uchida, and N. Miura, Physica B **201**, 427 (1994).
[35] M. Hirasawa, T. Ishihara, and T. Goto, J. Phys. Soc. Jpn. **63**, 3870 (1994).
[36] J. P. Perdew, K. Burke, and M. Ernzerhof, Phys. Rev. Lett. **77**, 3865 (1996).
[37] I. P. Swainson, R. P. Hammond, C. Soullière, O. Knop, and W. Massa, J. Solid State Chem. **176**, 97 (2003).
[38] C. G. Van de Walle and R. M. Martin, Phys. Rev. B **35**, 8154 (1987).
[39] T. Ishihara, J. Lumin. **60-61**, 269 (1994).
[40] J. M. Luttinger and W. Kohn, Phys. Rev. **97**, 869 (1955).
[41] G. Giorgi, J.-I. Fujisawa, H. Segawa, and K. Yamashita, J. Phys. Chem. Lett. **4**, 4213 (2013).
[42] R. Knox, *Theory of Excitons*, Solid State Physics: Supplement 5 (Academic Press, New York, 1963).

[43] K. Tanaka, T. Takahashi, T. Ban, T. Kondo, K. Uchida, and N. Miura, Solid State Commun. **127**, 619 (2003).

[44] V. D'Innocenzo, G. Grancini, M. J. P. Alcocer, A. R. S. Kandada, S. D. Stranks, M. M. Lee, G. Lanzani, H. J. Snaith, and A. Petrozza, Nat. Commun. **5**, 3586 (2014).

[45] L.-Y. Huang and W. R. L. Lambrecht, Phys. Rev. B **88**, 165203 (2013).

[46] J. T. Devreese and A. S. Alexandrov, Rep. Prog. Phys. **72**, 066501 (2009).

[47] C. Quarti, G. Grancini, E. Mosconi, P. Bruno, J. M. Ball, M. M. Lee, H. J. Snaith, A. Petrozza, and F. De Angelis, J. Phys. Chem. Lett. **5**, 279 (2014).

[48] L. Lang, J.-H. Yang, H.-R. Liu, H. Xiang, and X. Gong, Phys. Lett. A **378**, 290 (2014).